PHILOSOPHICAL TRANSACTIONS A

rsta.royalsocietypublishing.org

Research

Article submitted to journal

Subject Areas:
ocean engineering

Keywords:
tidal turbine, blade force, turbulent wake, experimental trials, PIV, POD

Author for correspondence:
Benoît Gaurier
e-mail: benoit.gaurier@ifremer.fr

Experimental analysis of the shear flow effect on tidal turbine blade root force from 3D mean flow reconstruction

B. Gaurier[1], Ph. Druault[2], M. Ikhennicheu[1] and G. Germain[1]

[1]IFREMER, Marine Structure Laboratory, 150 quai Gambetta, 62 200 Boulogne-sur-mer, France
[2]Sorbonne Université, CNRS UMR 7190, Institut Jean Le Rond d'Alembert, 75 005 Paris, France

In the main tidal energy sites like Alderney Race, turbulence intensity is high and velocity fluctuations may have significant impact on marine turbines. To understand such phenomena better, a three-bladed turbine model is positioned in the wake of a generic wall-mounted obstacle, representative of *in-situ* bathymetric variation. From 2D Particle Image Velocimetry planes, the time-averaged velocity in the wake of the obstacle is reconstructed in the three dimensional space. The reconstruction method is based on Proper Orthogonal Decomposition and enables access to a representation of the mean flow field and the associated shear. Then, the effect of the velocity gradient is observed on the turbine blade root force, for 4 turbine locations in the wake of the obstacle. The blade root force average decreases whereas its standard-deviation increases when the distance to the obstacle increases. The angular distribution of this phase-averaged force is shown to be non homogeneous, with variation of about 20 % of its time-average during a turbine rotation cycle. Such force variations due to velocity shear will have significant consequences in terms of blade fatigue.

1. Introduction

For the past ten years, many industrial projects have emerged in tidal energy harvesting all around the world. In Europe, there is a strong tidal energy potential, mainly located in the United Kingdom and France.

THE ROYAL SOCIETY PUBLISHING

Over 25 % of this European potential is located in the English Channel where currents with magnitude higher than $3\ m/s$ can be locally observed. However, such sites are often characterized with strong velocity variations [16]. The flow perturbations mainly come from waves or inflow turbulence due to coast or bathymetry effects [17]. As a consequence, marine turbines located in such areas undergo energetic and unsteady forcings, which especially apply to the blades, rotor, support structure and foundation. The power output exhibits then the signature of the turbulent coherent flow approaching the turbine. Ouro et Stoesser [17] performed numerical simulations with tidal turbine operating over an irregular bathymetry, i.e. above a train of dunes. They showed that the so-generated flow contains energetic large-scale turbulent structures, originated from this bathymetry, mainly in the form of roller and hairpin vortices. According to them, such structures have a profound impact on the tidal turbine, creating large fluctuations in the hydrodynamic loadings on the blades, being a potential risk of fatigue failure. These observations have recently been confirmed by *in-situ* measurements performed on a full-scale tidal turbine located in the Ramsey Sound, UK by Harrold and Ouro [13].

Ikhennicheu et al. [15] studied the wake of various elementary obstacles used to experimentally reproduce bathymetry variations, like those encountered in the Alderney Race in the middle of the English Channel. Such bathymetry variations have been observed *in-situ*, according to the geological description of this particular place presented by Furgerot et al. [7]. They concluded that a unique and wide obstacle, i.e. with an aspect ratio of 6, produces the most energetic wake that extends up to the free surface. In this case, large scale turbulent structures are periodically shed from its wake and can sometimes rise up to the surface and erupt to create a boil. The diameter of these vortices is similar to the one of a turbine at the same scale [14]. In order to know if such flow structures can be critical for tidal turbines behaviour, specific studies must be carried out. This work proposes to extend the existing database of the literature with the experimental study of a turbine response to the coherent turbulent wake of a wall-mounted square cylinder at a high Reynolds number of $Re = 2.5 \times 10^5$.

The main objectives of this present work are twofold. First, based on 2D PIV planes measurements, a method based on Proper Orthogonal Decomposition (POD) is proposed to reconstruct both mean velocity components in the three dimensional space. This enables a representation of the mean flow field and the associated shear mean flow that could impact a turbine whatever its location. The second objective of this work is to investigate the turbine response as a function of the shear mean flow from data obtained with a turbine positioned at four locations in the cylinder wake. In addition, the knowledge of the transverse characteristics of the flow is required to better understand the turbine response.

The paper is organized as follows. The first part deals with the experimental set-up and a brief description of PIV velocimetry measurement technique and turbine effort measurements. Then, the POD mathematical method allowing the 3D reconstruction of the mean flow field is described and the mean flow results are analysed. The third part presents the turbine response as a function of different mean shear flow and results are discussed.

2. Experimental set up and measurements

The tests have been carried out in the wave and current circulating flume tank of IFREMER located in Boulogne-sur-mer (France). The test section is: $18\ m$ long $\times$ $4\ m$ wide $\times$ $2\ m$ high. In this work, the three instantaneous velocity components are denoted (U, V, W) along the (X, Y, Z) directions respectively (Fig.1). Each instantaneous velocity component is separated into a mean value and a fluctuating part according to the Reynolds decomposition: $U = \overline{U} + u'$, where an overbar indicates the time average. The incoming flow generated by the flume tank far upstream from the wall-mounted cylinder is assumed to be steady and constant with $\overline{U_\infty} = 1\ m/s$ and $\overline{V_\infty} = \overline{W_\infty} = 0$ and with a turbulent intensity of $I_\infty = 1.5\ \%$.

The wall-mounted cylinder has an aspect ratio $A_R = \text{Width}/\text{Height} = 6$, as presented in [14]. It is representative of real-life conditions in Froude similitude and has the highest possible Reynolds

number (see table 1). As there is no obstacle upstream of the cylinder, the upstream flow is a simple boundary layer developing over the tank floor. Hence the experimental cylinder represents a bump considerably higher than its neighbours, producing some coherent flow structures as it could be encountered in the Alderney Race for instance [15]. For a cylinder height $H = 0.25\ m$, this element represents a key bathymetric element in the area of interest, at a 1:20 scale. In the following, all the quantities are non-dimensionalized by dividing by the cylinder height and indexed by *. At the obstacle position, the boundary layer height δ^* is calculated as $\delta^*_{95} = z^*(\overline{U} = 0.95\ \overline{U_\infty})$, given $\delta^* = 1.3$.

Table 1: *In-situ* and experimental conditions (1:20 scale): U_∞ stands for the far upstream velocity, H for the rugosity height, D_b for the water depth, R_e for the Reynolds number, F_r for the Froude number and D for the turbine diameter.

	Scale	U_∞	H	D_b	$R_e = \frac{HU_\infty}{\nu}$	$F_r = \frac{U_\infty}{\sqrt{gD_b}}$	D
	[-]	$[m/s]$	$[m]$	$[m]$	[-]	[-]	$[m]$
Alderney Race	1	5	5	40	2.5×10^7	0.25	$\simeq 15$
Flume tank	1/20	1	0.25	2	2.5×10^5	0.23	0.724

In previous works, the cylinder wake has been characterized from LDV and PIV measurements [14]. In this study, only the PIV database is used. This database is constituted of the 13 PIV measurement planes displayed on figure 1. These 13 PIV planes are repeated in the three transverse positions denoted y_0, y_1 and y_2 and corresponding to $y^* = [0; 1; 2]$ respectively. The plane y_0 is the cylinder longitudinal plane of symmetry. The PIV frame rate is 15 Hz.

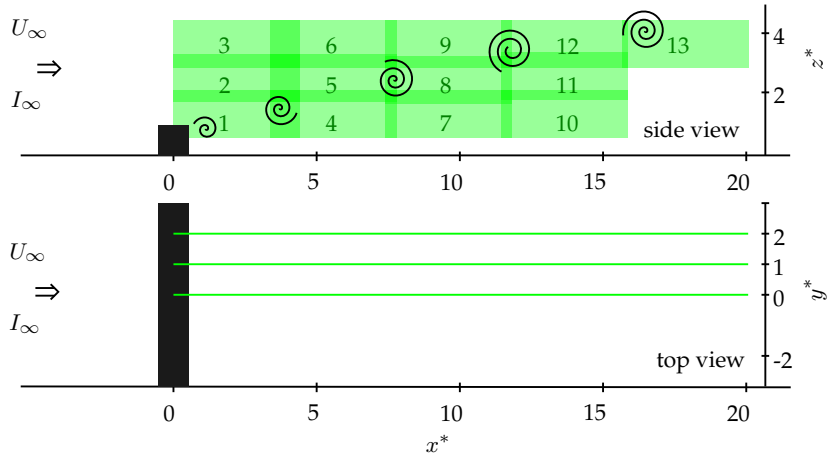

Figure 1: Side and top views of the PIV measurement planes locations in the wake of the wall-mounted cylinder. Origin is taken at the middle of the bottom face of the cylinder.

Average velocity maps of $\overline{U}$ and $\overline{W}$ in planes y_0, y_1 and y_2 are presented in figure 2. In these figures, the classical behaviour of the flow past a wall-mounted element can be observed: the flow separates at the leading edges of the cylinder into the outer steady region and the recirculation area downstream of the cube. A shear layer develops in-between and then the flow reattaches. The appearance of 3D effects mainly impacts planes for $y > y_1$: between y_0 and y_1 the recirculation length decreases by 8% and it decreases again by 18% between y_1 and y_2. Maps of the average vertical velocity $\overline{W}$ out of the symmetry plane indicate that the flow passing over the obstacle is

similar in the 3 planes for $x^* < 2$. However, downstream of the cylinder, the flow is considerably redirected towards the floor for position y_2 with a large and intense $\overline{W} < 0$ zone. This database is used in section 3 for the 3D mean flow reconstruction.

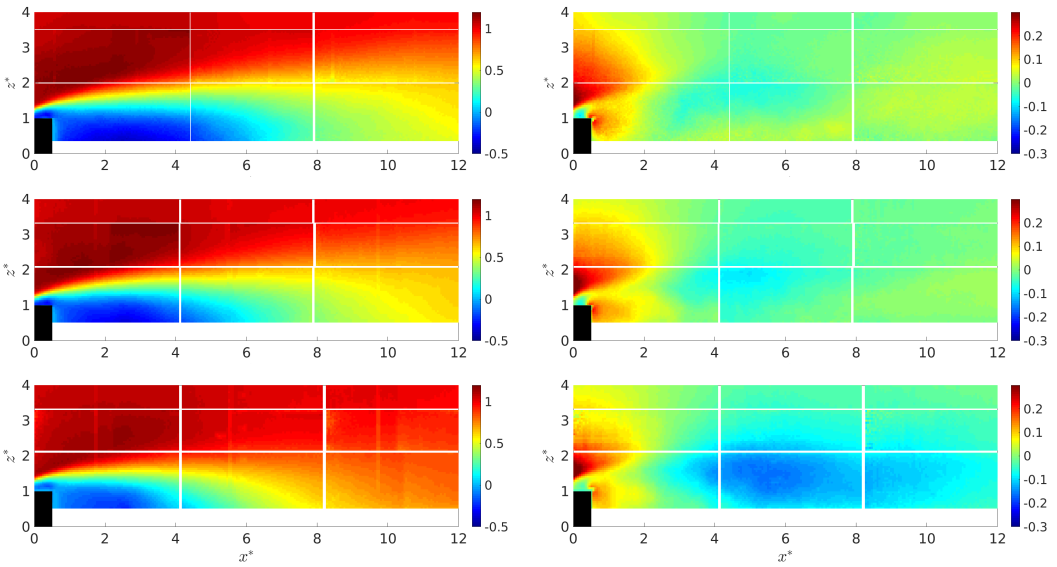

Figure 2: $\overline{U}/U_\infty$ (left) and $\overline{W}/U_\infty$ (right) maps in plane y_0 (top), y_1 (middle) and y_2 (bottom). White parts indicate the different PIV measurement planes separation.

A three-bladed horizontal axis turbine of diameter $D = 0.724\ m$ is positioned in the cylinder wake at mid-depth of the tank ($z^* = 4$) and at four different downstream positions $x^* = [4; 10; 16; 23]$, as presented on figures 3 and 4. This turbine has been developed at IFREMER and was first presented in [11]. The turbine blades are rigid and their open geometry is described in [10]. When the turbine is rotating, its speed is controlled and the blade pitch does not change. Each blade root is equipped with a specific load-cell including 5 different channels: 2 forces (F_{xi} and F_{yi}) and 3 moments (M_{xi}, M_{yi} and M_{zi}, $i = 1, 2, 3$). The torque (Q) and the thrust (T) applied on the main rotation axis are also measured. The rotation direction is depicted on schematic 3 with the angle $\theta = 0°$ corresponding to the blade B1 at the top dead centre.

In this study, the turbine rotation will be considered at the nominal operating point, which is the point at which the output power is maximised. In the present set-up for which the TSR similitude is used, that point is at $TSR = 4$, as shown in [10]. It is reminded that $TSR = \frac{\Omega R}{U}$ with Ω the angular velocity and $R = D/2$ the turbine radius.

From these four turbine locations, it will be possible to investigate the turbine response as a function of the shear mean flow. This analysis will be facilitated by the reconstruction of both mean velocity components in the three dimensional space as presented hereafter.

3. 3D Mean flow reconstruction

Based on 2D PIV measurement plane orthogonal to the main flow direction, previous works have reconstructed the 3D flow velocity field with the assumption of frozen turbulence via Taylor hypothesis [8]. A more advanced technique called "snapshot optimisation" based on Proper Orthogonal Decomposition (POD) has been recently applied to a two orthogonal PIV plane measurement database to reconstruct the large scale structures of turbulent flow presenting a direction of homogeneity (wake, mixing layer, etc.) [3]. To reconstruct large scale flow structures of a jet, Hamdi et al [12] performed stereoscopic PIV measurements and applied POD to each of the

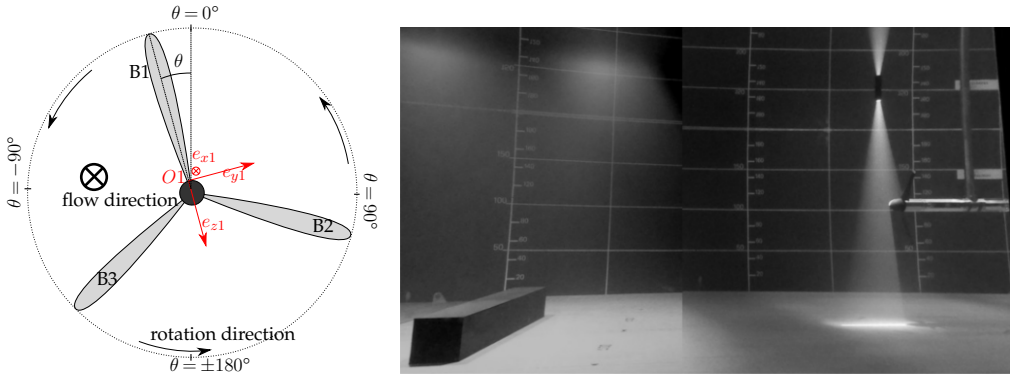

Figure 3: Schematic of the turbine facing the flow with the angle of rotation θ orientation and the blade B1 coordinate system (left) and picture of the experimental set-up with the cylinder and the turbine located at $x^* = 10$ (right).

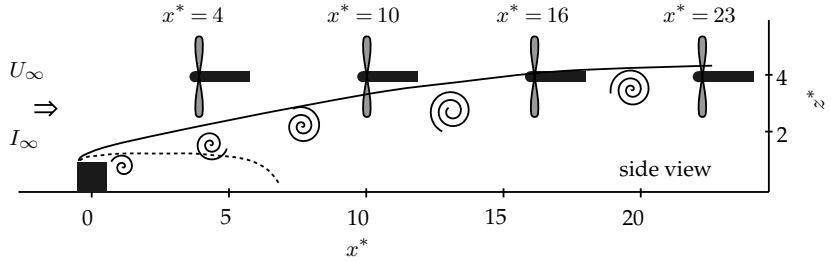

Figure 4: Schematic representation of the experimental set-up with the cylinder and the turbine located at the four positions $x^* = [4; 10; 16; 23]$ in the cylinder wake extension. The black line stands for the wake extension: $\overline{U} = 0.9 \times \overline{U}_\infty$ and the dotted line represents the recirculation zone: $\overline{U} < 0$. The turbine is always centred at mid depth ($z^* = 4$).

measured plane. Then, by extracting the most energetic POD modes in each plane, the energetic flow structures are reconstructed in the volume study based on a POD interpolation. POD has been also used as a temporal interpolation tool to access the large scale flow dynamics of an in-cylinder engine flow [5] and to reconstruct spatial missing data [2]. This solves a linear equation established from partial observations for the desired flow field. In a similar way, Qamar and Sanghi [19] proposed an application of POD approach to a range of parameter values that permits to predict the mean flow field within a parameter set. From 2D PIV measurements performed in orthogonal measurement planes, Druault and Chaillou [6] obtained the 3D mean velocity field using POD method for in-cylinder engine flow.

Following previous works, POD is used here as a tool for reconstructing the mean velocity field in the 3D space by using 2D PIV velocity vectors obtained in several parallel planes. The purpose of POD applied to a discrete data set of a flow variable u is to decompose this data set as a linear combination of orthonormal eigenfunctions (spatial modes, denoted $\Phi^{(n)}(x,z)$) and associated temporal coefficients denoted $a^{(n)}(t)$: $u(x,z,t) = \sum_{n=1}^{N_{mod}} a^{(n)}(t)\Phi^{(n)}(x,z)$ with N_{mod} the total number of POD modes. This decomposition is optimal in the sense that eigenfunctions contain as much energy as possible. When dealing with fluctuating velocity field database, the energy corresponds to the turbulent kinetic energy which is mainly contained in the large scale flow structures. That permits the extraction of these flow structures from a combination of the first POD modes (the first mode reproducing the mean flow).

(a) Reconstruction procedure of the mean velocity field

In the following, each measurement plane depicted on figure 1 is denoted p_i with i varying from 1 to 13. These planes are repeated three times for the three transverse positions (y_0, y_1 and y_2) but always keep the same (x, z) coordinates whatever the transverse position. In each plane, $N_t = 2249$ instantaneous velocity vectors are obtained on a regular meshgrid of $(N_x \times N_z)$ points. The vectorial POD method is implemented in the mathematical procedure, simultaneously accounting for both velocity components. For clarity, the classical scalar POD method applied to u velocity component only is detailed below in 5 main steps:

(i) The three instantaneous velocity fields $u^{p_i}(x, z, y_0, t)$, $u^{p_i}(x, z, y_1, t)$ and $u^{p_i}(x, z, y_2, t)$ are concatenated into a single matrix $U = [u^{p_i}(x, z, y_0, t), u^{p_i}(x, z, y_1, t), u^{p_i}(x, z, y_2, t)]$. This matrix is of size $[N_x \times N_z, N_y \times N_t]$. The PIV measurements in planes y_0, y_1 and y_2 are not obtained simultaneously and time variable t differs from one plane to another one.

(ii) The classical POD is applied to matrix U. It allows to obtain $N_{mod} = N_x \times N_z$ POD spatial eigenfunctions $\Phi^{(n)}(x, z)$ of size (N_x, N_z) and N_{mod} POD temporal coefficients $a^{(n)}(t)$ of size $(N_t \times N_y)$ deduced from the projection of U onto $\Phi^{(n)}(x, z)$. These temporal coefficients are re-organized as follows $[a_0(y_0, N_t)\, a_1(y_1, N_t)\, a_2(y_2, N_t)]$ with each vector a_i is of size N_t. POD leads to the following exact reconstruction, with $j \in [0:2]$:

$$u^{p_i}(x, z, y_j, t) = \sum_{n=1}^{N_{mod}} a_j^{(n)}(t)\, \Phi^{(n)}(x, z) \tag{3.1}$$

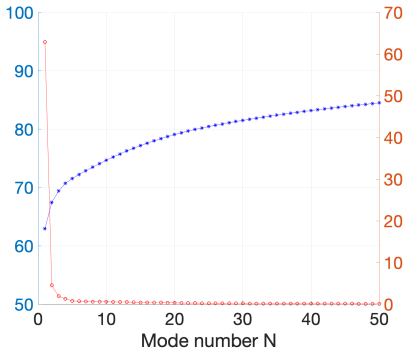

(a) Mode energy convergence, expressed in percentage value. Blue: cumulative POD mode content $\sum_{i=1}^{N} \lambda^{(i)} / \sum_{n=1}^{N_{mod}} \lambda^{(n)}$ (left y-axis). Red: POD mode energy content $\lambda^{(N)} / \sum_{n=1}^{N_{mod}} \lambda^{(n)}$ (right y-axis).

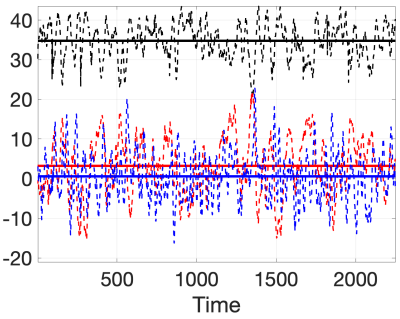

(b) Time evolution of the first three POD coefficients $a_0^{(n)}(t)$ in plane y_0. POD mode number n varying from 1 to 3: 1 (black), 2 (red) and 3 (blue).

Figure 5: POD of measurement plane #1 results.

Figure 5a presents the POD energy convergence, limited to 50 (among the N_{mod} modes) to better see the convergence. The first POD mode contains $\approx 63\%$ of the total energy and high order POD modes superior to 5 contain less than $\approx 0.5\%$. An illustration of the time evolution of the first three temporal coefficients $a_0^{(n)}(t)$ with $n \in [1:3]$ is displayed in figure 5b. In this figure, the time average of each coefficient is also represented as a line. The mean values $\overline{a_i^{(n)}}$ converge quickly to zero value as mode number n increases confirming that high order POD modes are linked to the fluctuating part of the velocity

field. The first 5 spatial eigenfunctions are plotted in figure 6. It is observed that for $n \geq 5$, spatial eigenfunctions $\Phi^{(n)}(x,z)$ are more noisy suggested that they are more related to the fluctuating velocity field.

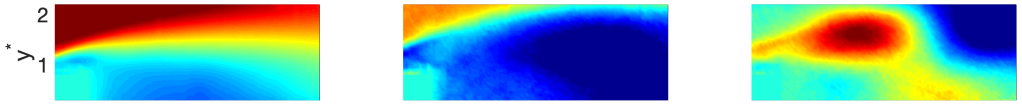

(a) $\Phi^{(1)}(x,z)$, $\Phi^{(2)}(x,z)$ and $\Phi^{(3)}(x,z)$

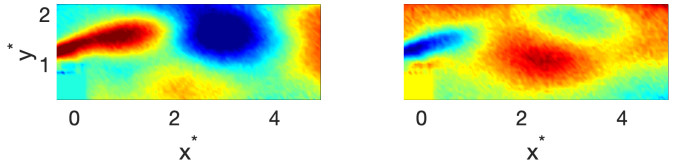

(b) $\Phi^{(4)}(x,z)$ and $\Phi^{(5)}(x,z)$

Figure 6: First five spatial POD modes for plane #1. The colormap is from -0.04 (blue) to 0.03 (red)

(iii) The mean velocity flow field is computed in each transverse section y_i. This part consists in determination of the number $M < N_{mod}$ satisfying: $\overline{U(x,z,y_i)} = \sum_{n=1}^{M} \overline{a_i^{(n)}} \Phi^{(n)}(x,z)$, whatever y_i plane. The M parameter sensitivity has been studied by comparing the reconstructed mean velocity fields inside the volume to the 2D mean velocity fields coming from the measurements. For each p_i plane ($i \in [1:13]$) there was no difference between $M=5$ and $M=6$ or even between $M=4$ and $M=5$ for some of the planes. In this last case, keeping $M=5$ instead of $M=4$ does not change the reconstruction stage because the average value of the 5th POD coefficient is close to zero (lower than 10^{-3}). Finally, $M=5$ seems to be a good compromise to retrieve the classical mean flow in each of the three measurements plane.

(iv) The POD temporal coefficients are spatially interpolated along the transverse direction. For this study, the interpolation is performed between the three PIV measurement planes. After calculating the mean of the POD coefficients, for each POD mode number varying from 1 to M, the temporal coefficients are interpolated (cubic spline interpolation) at any y location between y_0 and y_2 that is $y^* \in [0:2]$. They are denoted $\overline{a^{(n)rec.}(y)}$.

(v) It is then possible to reconstruct the mean flow in the 3D space from the following equation:

$$\overline{U(x,y,z)} = \sum_{n=1}^{M} \overline{a^{(n)rec.}(y)} \Phi^{(n)}(x,z). \tag{3.2}$$

A previous study showed that the mean transverse velocity is of zero value in the symmetrical plane y_0 [14] and it is expected that both other mean velocity components are symmetrical with respect to the symmetrical y_0-axis of the cylinder. Then, applied this symmetrical condition, the mean flow field is reconstructed within the interval $y^* \in [-2:2]$.

The interest of such reconstruction procedure is that only the mean POD coefficients are space-interpolated and original spatial POD eigenfunctions $\Phi^{(n)}(x,y)$ remain the same.

(b) Mean flow reconstruction

The same procedure is conducted for each of the 13 available PIV planes in each transverse section y_0 to y_2 (figure 1). Figure 7 illustrates this reconstruction for selected areas along the x-axis.

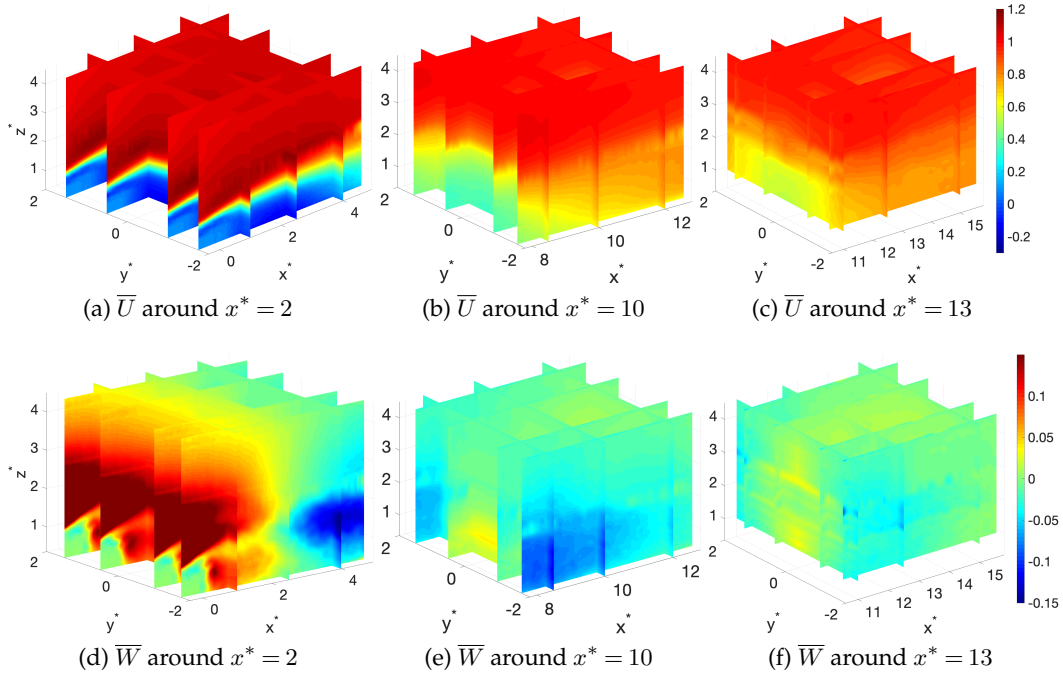

(a) $\overline{U}$ around $x^* = 2$ (b) $\overline{U}$ around $x^* = 10$ (c) $\overline{U}$ around $x^* = 13$

(d) $\overline{W}$ around $x^* = 2$ (e) $\overline{W}$ around $x^* = 10$ (f) $\overline{W}$ around $x^* = 13$

Figure 7: Illustration of the 3D reconstruction of both mean velocity components at different position in the wake of the obstacle

For figures 7a and 7d, the reconstruction of $\overline{U(x,y,z)}$ and $\overline{W(x,y,z)}$ is obtained from database in measurement planes #1, #2 and #3, that is for $x^* \in [-0.5 : 4.5]$. The centre figures 7b and 7e corresponds to measurement planes #7, #8 and #9, that is for $x^* \in [7.8 : 12.5]$ and the right figures 7c and 7f are related to measurement planes #10, #11 and #12, that is for $x^* \in [10.8 : 15.5]$ (see figure 1 for planes numbering). A similar colormap is used for each velocity component. In the near wake, a recirculation area downstream the cylinder is observed. This recirculation area is still visible for $x^* > 8$ (centre graph) for the $\overline{U}$ velocity component. This area is more intense around the symmetrical y_0-axis. It is also quite interesting to note the $\overline{U}$ acceleration at the top of the shear layer. Moreover, the magnitude of the $\overline{U}$ decreases as we move downstream from the cylinder, along the same height $z^* \approx 4$.

On the other hand, the edge effects of the cylinder are clearly visible when looking at the $\overline{W}$ velocity component. Downstream of the cylinder, the flow is considerably redirected towards the floor at the limit of the transverse domain $y^* \approx \pm 2$ with a large and intense $\overline{W} < 0$ zone.

To further investigate the mean flow field and especially the shear flow, figure 8 represents the reconstructed $\overline{U}$ and $\overline{W}$ components in the streamwise sections where the turbine will be positioned. The inflow that the turbine will encounter is emphasized by the representation of the blades swept area (dashed lines). Table 2 indicates the range of variation of the mean streamwise velocity component $\overline{U}$ and of the 2D turbulent kinetic energy $k = \frac{1}{2}(\overline{u'^2} + \overline{w'^2})$, along the z direction between the bottom tip ($z^* = 2.5$) and the top tip ($z^* = 5$) of the rotor, for the four downstream locations.

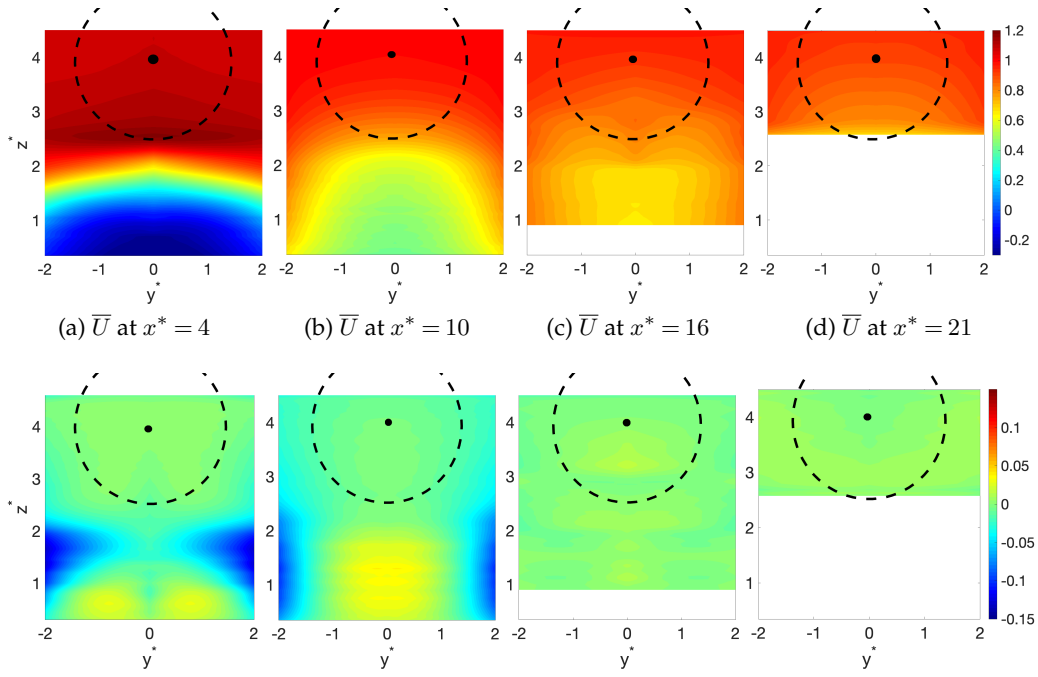

(a) $\overline{U}$ at $x^* = 4$ (b) $\overline{U}$ at $x^* = 10$ (c) $\overline{U}$ at $x^* = 16$ (d) $\overline{U}$ at $x^* = 21$

(e) $\overline{W}$ at $x^* = 4$ (f) $\overline{W}$ at $x^* = 10$ (g) $\overline{W}$ at $x^* = 16$ (h) $\overline{W}$ at $x^* = 21$

Figure 8: Mean streamwise $\overline{U}$ (top) and spanwise $\overline{W}$ (bottom) velocity components in each streamwise section under interest. Dashed lines depict the turbine blades swept area. Note that the last section of the reconstructed velocity volume is $x^* = 21$ whereas the last turbine position is $x^* = 23$.

Table 2: Range of variation of the mean streamwise velocity component $\overline{U}$ and of the normalized 2D turbulent kinetic energy $k^* = \frac{1}{2}(\overline{u'^2} + \overline{w'^2})/U_\infty^2$, along the z direction (and at $y^* = 0$) between the bottom tip ($z^* = 2.5$) and the top tip ($z^* = 5$) of the rotor, for the four downstream locations.

x^*	$\overline{U}_{top}\ [m/s]$	$\overline{U}_{bottom}\ [m/s]$	$k^*_{top}\ (\times 10^{-3})$	$k^*_{bottom}\ (\times 10^{-3})$
4	1.07	1.18	5.4	14.5
10	1.01	0.78	1.7	51.0
16	0.98	0.76	1.7	30.0
21	0.99	0.72	4.0	17.5

In each position, the main shear is observed along the vertical direction for the $\overline{U}$ component. The $\overline{W}$ component is not subjected to noticeable shear compared to the other velocity component. For $x^* = 4$ (in the near wake), $\overline{U}$ is maximal at the bottom of the turbine swept area: $1.18\ m/s$ against $1.07\ m/s$ at the top tip of the rotor. The shear is inverted due to the acceleration caused by the obstacle blockage, compared to the shear observed in other streamwise locations. Indeed, as we move downstream, the flow is dissipated and the bottom of the turbine will be subjected to low $\overline{U}$ velocity compared to the one imposed at the top tip of the turbine (table 2). Moreover, when going downstream, the magnitude of the mean $\overline{U}$ component is reduced. Note that the vertical turbulent kinetic energy gradient observed on table 2 may also have some effects on the turbine performance. In this study however, the 2D turbulent kinetic energy is only available along a z-line and the 3D kinetic energy may vary in the rotor swept area as well. Future studies have to be carried out to investigate such an effect. Based on the knowledge of the mean flow velocity field

in the whole volume of study, the effect of the mean shear flow onto the blade root force of the turbine can be examined.

4. Shear flow effect on turbine blade root force

On figure 9 is displayed a temporal extract of F_{x1}, for the 4 positions of the turbine. For the first position ($x^* = 4$), the fluctuations F'_{x1} around the time average value $\overline{F_{x1}}$ are always lower than $5\ N$. From the second position ($x^* = 10$), large amplitude peaks are visible, which can locally reach several tens of N. The number of these peaks increases with the distance to the cylinder: 3 to 4 in 20 s for $x^* = 10$ and about 15 for $x^* = 23$. In addition, these forces clearly show periodic fluctuations at the rotation frequency. When a vortex passes, the amplification of these periodic fluctuations is due to the instantaneous increase of the shear in the velocity profile. This phenomena will have a significant impact on the structural fatigue of the blades, when occur at real scale.

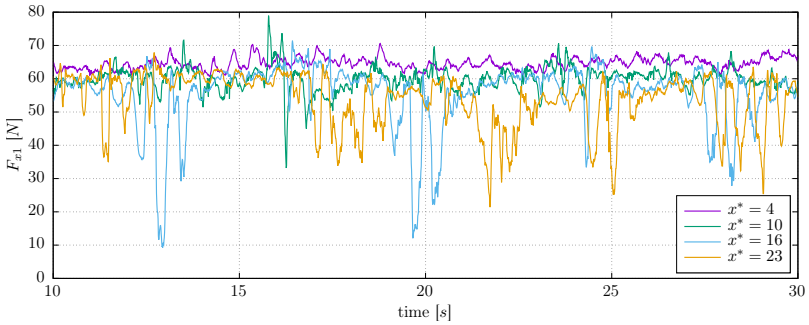

Figure 9: F_{x1} temporal extract for the 4 positions of the turbine in the wake of the cylinder

$\overline{F_{x1}}$ is higher for $x^* = 4$, comparing to $x^* = 23$ with decreasing values when increasing the distance. The statistical values measured for F_{x1} are given in table 3 for the 4 positions of the turbine. These values confirm the decreasing of the time average when the distance increases, from $65\ N$ to $54\ N$ respectively for $x^* = 4$ and $x^* = 23$. In addition, the standard-deviation is maximum at $x^* = 16$, with $\sigma(F_{x1}) = 9\ N$. However, because the standard-deviation disables to properly show the large peaks observed on figure 9, minimum and maximum are added to the table 3 as well. The largest amplitudes between minimum and maximum are reached for $x^* = 10$ and $x^* = 16$ with $73\ N$ for both distances. For $x^* = 23$, the difference between minimum and maximum is $57\ N$.

Table 3: Streamwise component of the reconstructed velocity spatially averaged over the turbine swept area $\overline{U}$ and time average, standard-deviation, minimum and maximum of F_{x1} for the 4 positions of the turbine in the wake of the cylinder. Values are expressed in m/s for U and in N for F_{x1}. Note that the last section of the reconstructed velocity is $x^* = 21$ whereas the last turbine position is $x^* = 23$.

x^*	$\overline{U}$	$\overline{F_{x1}}$	$\sigma(F_{x1})$	min(F_{x1})	max(F_{x1})
4	1.09	64.7	1.8	59.0	74.5
10	0.98	59.6	5.1	8.3	81.3
16	0.93	55.0	9.0	1.6	74.6
21/23	0.89	53.6	8.3	14.6	71.4

These remarks on the blade B1 root force are in agreement with the reconstructed average velocities displayed on figure 8 and given on tables 2 and 3. The average velocity is the highest

at $x^* = 4$ and then decreases with the distance. This mainly explains the previously described evolution of the time average $\overline{F_{x1}}$ with the distance. Furthermore, as previously noticed the velocity gradient perceived by the turbine is reversed between position $x^* = 4$ and the three others: the lowest velocities are located in the bottom part of the rotor swept area for positions $x^* = 10$ to $x^* = 23$, whereas these are the highest velocities for position $x^* = 4$. This shear is responsible of the periodic component already noticed on F_{x1}, at the rotation frequency. From the shear, vortices are emitted and pass through the blade swept area. They locally and shortly amplify the vertical velocity gradient perceived by the blades, creating larger peaks. Because the gradient is inverted between $x^* = 4$ and the three other positions, these peaks tend to be positive for $x^* = 4$ and are mainly negative for the other positions. Finally, the amplitude of these peaks depends on the distance to the cylinder: for $x^* = 4$ vortices are mainly under the rotor swept area whereas they start to reach the blade from $x^* = 10$.

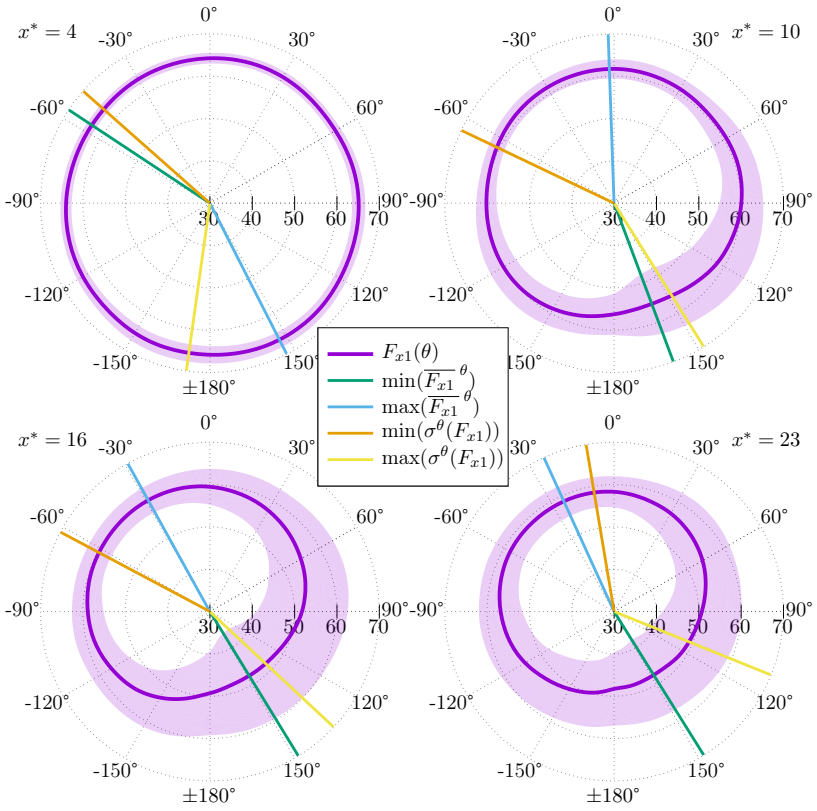

Figure 10: Angular phase average $\overline{F_{x1}}^{\theta}$ and standard-deviation $\sigma^{\theta}(F_{x1})$ of blade B1 force F_{x1} for the 4 turbine positions in the wake of the cylinder, with their corresponding minima and maxima angles. Values are expressed in N.

In order to better understand the effect of the shear on the turbine blades, we propose to study the angular load distribution. On figure 10 are displayed the angular phase average $\overline{F_{x1}}^{\theta}$ and standard-deviation $\sigma^{\theta}(F_{x1})$ of the force F_{x1} for the 4 positions of the turbine ($\theta = 0°$ corresponds to blade B1 at the top dead centre as shown on figure 3). Corresponding forces for blades B2 and B3 are not displayed in this figure for clarity reasons and because their results are very similar to blade B1, with $\pm 120°$ difference. Furthermore, the angular positions of the maxima and minima of both these quantities are shown on this figure with coloured lines. They are given in table 4 as well with their corresponding force values.

Table 4: Angles of the minima and maxima of the angular phase average $\overline{F_{x1}}^{\theta}$ and standard-deviation $\sigma^{\theta}(F_{x1})$ of the blade B1 force F_{x1} for the 4 turbine positions. Angles are expressed in degree and values are expressed in N.

x^*	$\min(\overline{F_{x1}}^{\theta})$		$\max(\overline{F_{x1}}^{\theta})$		$\min(\sigma^{\theta}(F_{x1}))$		$\max(\sigma^{\theta}(F_{x1}))$	
	angle	value	angle	value	angle	value	angle	value
4	-57	63.4	154	66.2	-49	1.2	-171	2.1
10	160	55.4	-2	61.7	-65	1.9	148	7.8
16	149	47.8	-29	60.0	-62	3.0	133	11.9
23	148	47.6	-25	58.6	-10	3.6	112	9.9

As already observed on figure 9, the highest average is reached when the turbine is positioned at the closest location to the obstacle: $x^* = 4$. For this position, $\overline{F_{x1}}^{\theta}$ is rather homogeneously distributed versus the turbine angle: the minimum is $63.4\ N$ for $\theta = -57°$ and the maximum is $66.2\ N$ for $\theta = 154°$. On the contrary, the lowest averaged is observed for the highest distance: $x^* = 23$. For this last position, the minimum is $47.6\ N$ for $\theta = 148°$ and the maximum is $58.6\ N$ for $\theta = -25°$. The difference between maximum and minimum is then $11\ N$. However, because the turbine rotation is $TSR = 4$, one rotation cycle lasts $0.58\ s$. That means during each turbine rotation cycle, or every $0.58\ s$, the variation amplitude of the phase average $\overline{F_{x1}}^{\theta}$ is $11\ N$. This difference is even higher for position $x^* = 16$ (figure 10) with more than $12\ N$. Accounting for the time-average given in table 3, $\overline{F_{x1}} = 55\ N$, which gives angular variations higher than 20 % of the time average for this position. Such cyclical force variation in a quite short time can affect the blade and rotor fatigue [4,21]. In addition, the angular position of the minima and maxima of the average force is different between the first position and the others. Maxima are around $\theta = -30°$ and minima are at the opposite direction, *i.e.* around 150°, for $x^* = 10$, 16 and 23. For position $x^* = 10$, maximum and minimum angles are not really accurate because the angular gradient is smoother and less pronounced than the ones for the two last positions. However, minimum is obtained at about -60° and maximum at about 150° for the first position. This result is in opposition to the three other positions. This remark can be explained by the reconstructed streamwise velocity component gradient presented previously on figure 8 and table 2, where the bottom part of the turbine swept area is marked by the highest velocities for position $x^* = 4$ and by the lowest ones for the other positions. According to these results, it would have been expected that minimum and maximum angles should have been 0° and 180° (respectively 180° and 0° for $x^* = 10$, 16 and 23). According to these results, a phase delay of about -30° is clearly noticeable in this study.

On the contrary to the average, the standard-deviation of the F_{x1} force tends to increase with the distance to the obstacle. For the first position, it stays quite low with a maximal value of $2.1\ N$ at $\theta = -171°$. The highest value is reached at the position $x^* = 16$ with $11.9\ N$ at $\theta = 133°$. For every position, the maximum of the standard-deviation is always between 180° and 120°, *i.e.* around $\theta = 150°$. Again, this can be explained by the location of the strongest velocity gradient as seen on figure 8 and table 2 with the reconstructed velocity, which is always at the bottom part of the turbine swept area, accounting for the -30° phase delay previously observed for the average load evolution. Such phase lag is already experimentally noticed by other authors when turbine is submitted to a vertically sheared flow, e.g. by Ahmed et al. [1] and Payne et al. [18] for real-scale and model-scale tidal turbines respectively. According to Gao et al. [9] who recently observed the same phenomenon on a large-scale wind turbine, this phase lag is due to rotational effects. Finally, Shen et al. [20] numerically studied the azimuthal fluctuating loads of a wind turbine arisen from wind shear. They attributed such a phase lag to an asymmetry of wake structure of the blade. Indeed, the velocity shear creates additional fluctuation of the force when the blade goes through it, due to a temporary change in the flow regime and in the effective angle of attack of the blade profile. Further investigations on this subject seem however to be required.

5. Conclusion

This study presents some results from an experimental campaign focused on the behaviour of a three-bladed horizontal axis tidal turbine model submitted to a turbulent flow generated by the wake of a generic wall-mounted obstacle. This obstacle is representative of the bathymetric variations encountered in the Alderney Race. Previous studies showed that large scale turbulent structures can be periodically shed in the wake of such obstacles, with a size comparable to the diameter of the turbine model. The turbine is successively positioned at four downstream locations in the wake of the cylinder. However, to understand the turbine results better, it is necessary to accurately characterize this turbulent flow out of the symmetry plane.

A velocity reconstruction method is proposed in this paper using the POD applied on both velocity components of several 2D PIV planes measurements, initially performed without the turbine. This reconstruction method enables the mean flow field as well as its associated shear to be accessed in the wake of the obstacle and in the three dimensional space. The method is constituted of the following steps: (i) the POD is processed on the velocities to obtain the spatial eigenfunctions and temporal coefficients, (ii) the first temporal coefficients are spatially interpolated along the different transverse measurement positions, (iii) the mean flow is finally reconstructed from the interpolated temporal coefficients associated with their corresponding eigenfunctions, on the volume of interest. The interest of this method mainly lies in the interpolation of a finite number of temporal coefficients only. Some details appear more clearly downstream from the obstacle: e.g. the recirculation area, the streamwise acceleration at the top of the shear layer, the decrease of the streamwise component of the velocity at mid-depth or the edge effects of the obstacle from the spanwise component of the velocity. From the reconstructed volume, the four streamwise sections corresponding to the four turbine locations can be extracted. The shear flow can eventually be characterized: it is mainly observed along the vertical direction and for the streamwise component only. For the first turbine position, the velocity is maximal at the bottom of the turbine. On the contrary, for the other positions, the bottom of the turbine is subjected to the lowest velocity.

The effect of such velocity gradients is observed on the turbine blade root force analysis. The presence of the shear associated with flow structures creates a periodic fluctuation in this load at the rotation frequency. Furthermore, when a vortex passes through the turbine swept area, the instantaneous increase of the shear amplifies this periodic fluctuation creating large amplitude peaks. This phenomenon is stronger and more frequent when the distance of the turbine to the obstacle increases. The angular distribution of the phase-average force has been shown to be non homogeneous. As observed on the reconstructed shear velocity, the highest average is reached close to the bottom for the first position and close to the top for the three other positions. However, these top and bottom positions of the blades are not at 0° and 180° as expected, but appear with a phase delay of about -30°. This phase lag requires additional investigations to understand its origin better, but seems to be linked to rotational effects and to an asymmetry of the wake structure of the blade. The difference between the phase average maximum and minimum of this blade force during a turbine rotation cycle is higher than $10\ N$ for the two furthest turbine locations. With a time average of about $50\ N$, that means about 20 % of average variation for every rotation cycle. Such force variations due to velocity shear will have significant consequences in terms of blade fatigue.

Data Accessibility. The corresponding raw data are available on the SEANOE plateform.

Authors' Contributions. B. Gaurier and M. Ikhennicheu carried out the experiments. Ph. Druault performed the mean flow reconstruction and drafted the corresponding section of the manuscript. G. Germain conceived of the study. B. Gaurier and M. Ikhennicheu performed the turbine model data analysis. B. Gaurier and G. Germain drafted the rest of the manuscript. All authors read and approved the manuscript.

Competing Interests. The authors declare that they have no competing interests.

Funding. This work benefits from a French State grant managed by the National Research Agency under the Investments for the Future program bearing the reference ANR-10-IEED-0006-11. This project was partly

financially supported by the European Union (FEDER), the French government, IFREMER and the region Hauts-de-France in the framework of the project CPER 2015–2020 MARCO. This work also received the support of the MET-CERTIFIED project, funding from the Interreg 2 Seas programme 2014–2020 and co-funded by the European Regional Development Fund under subsidy contract 2S01–020.

Acknowledgements. The authors are most grateful to Thomas Bacchetti, Inès Belarbi and Jean-Valery Facq.

References

1. Ahmed U., Apsley D.D., Afgan I., Stallard T. and Stansby P.K. 2017 Fluctuating loads on a tidal turbine due to velocity shear and turbulence: Comparison of CFD with field data. *Renewable Energy* **112** 235–246.
2. Bui-Thanh T., Damodaran M. and Willcox K. 2004 Aerodynamic Data Reconstruction and Inverse Design Using Proper Orthogonal Decomposition. *AIAA J.* **42-8** 1505–1516.
3. Chandramouli P., Memin E., Heitz D. and Fiabane L. 2019 Fast 3D flow reconstructions from 2D cross-plane observations. *Exp. Fluids* **60-2** 30.
4. Davies P., Germain G., Gaurier B., Boisseau A. and Perreux D. 2013 Evaluation of the durability of composite tidal turbine blades. *Phil Trans R Soc A* **371** 20120187.
5. Druault Ph., Guibert P. and Alizon F. 2005 Use of Proper Orthogonal Decomposition for time interpolation from PIV data. *Exp. Fluids* **39-6** 1009–1023.
6. Druault Ph. and Chaillou C. 2007 Use of Proper Orthogonal Decomposition for reconstructing the 3D in-cylinder mean-flow field from PIV data. *CR. Mecanique* **335**(1) 42–47.
7. Furgerot L., Poprawski Y., Violet M., Poizot E., Bailly du Bois P., Morillon M. and Mear Y. 2019 High-resolution bathymetry of the Alderney Race and its geological and sedimentological description (Raz Blanchard, northwest France). *Journal of Maps* **15**(2) 708–718.
8. Ganapathisubramani B., Lakshminarasimhan K. and Clemens NT. 2007 Determination of complete velocity gradient tensor by using cinematographic stereoscopic PIV in a turbulent jet. *Exp. Fluids* **42-6** 923–939.
9. Gao L., Yang S., Abraham A. and Hong J. 2020 Effects of inflow turbulence on structural response of wind turbine blades. *J. of Wind Eng. and Ind. Aero.* **199** 104137.
10. Gaurier B., Germain G., Facq J.-V., Johnstone C., Grant A., Day A., Nixon E., Di Felice F. and Costanzo M. 2015 Tidal energy "Round Robin" tests comparisons between towing tank and circulating tank results. *International Journal of Marine Energy* **109** 12–87.
11. Gaurier B., Germain G. and Facq J.-V. 2017 Experimental study of the Marine Current Turbine behaviour submitted to macro-particle impacts. In: proceedings of the 12th European Wave and Tidal Energy Conference (EWTEC). Cork, Ireland. *EWTEC*
12. Hamdi J., Assoum H., Abed-Meraïm K. and Sakout A. 2018 Volume reconstruction of an impinging jet obtained from stereoscopic-PIV data using POD. *Euro. J. Mech. B-Fluids* **67** 433–445.
13. Harrold M. and Ouro P. 2019 Rotor loading characteristics of a full-scale tidal turbine. *Energies* **12**(6) 1–19.
14. Ikhennicheu M., Germain G., Druault Ph. and Gaurier B. 2019 Experimental study of coherent flow structures past a wall-mounted square cylinder. *Ocean Engineering* **182** 137–146.
15. Ikhennicheu M., Germain G, Druault Ph. and Gaurier B. 2019 Experimental investigation of the turbulent wake past real seabed elements for velocity variations characterization in the water column. *International Journal of Heat and Fluid Flow* **78** 108426.
16. Myers L. and Bahaj A. 2005 Simulated electrical power potential harnessed by marine current turbine arrays in the Alderney Race. *Renewable Energy* **30** 1713–1731.
17. Ouro P. and Stoesser T. 2019 Impact of Environmental Turbulence on the Performance and Loadings of a Tidal Stream Turbine. *Flow, Turbulence and Combustion* **102** 613–639.
18. Payne G., Stallard T., Martinez R. and Bruce T. 2018 Variation of loads on a three-bladed horizontal axis tidal turbine with frequency and blade position. *J. Fluids Struct.* **83** 156–170.
19. Qamar A. and Sanghi S. 2009 Steady supersonic flow-field predictions using proper orthogonal decomposition technique. *Computers & Fluids* **38** 1218–1231.
20. Shen X., Zhu X. and Du Z. 2011 Wind turbine aerodynamics and loads control in wind shear flow. *Energy* **36** 1424–1434.
21. Suzuki T. and Mahfuz H. 2018 Fatigue characterization of GFRP and composite sandwich panels under random ocean current loadings. *International Journal of Fatigue* **111** 124–133.